

# Tracking the photoinduced dynamics of a dark excitonic state in single-layer WS<sub>2</sub> via resonant Autler-Townes splitting

Angela Montanaro<sup>1,2,3,\*</sup>, Francesco Valiera<sup>4,\*</sup>, Francesca Giusti<sup>1,2</sup>, Francesca Fassioli<sup>3</sup>, Chiara Trovatello<sup>5,6</sup>, Giacomo Jarca<sup>1,2,3</sup>, Enrico Maria Rigoni<sup>1,2,3</sup>, Fang Liu<sup>7,8</sup>, Xiaoyang Zhu<sup>7</sup>, Stefano Dal Conte<sup>5</sup>, Giulio Cerullo<sup>5,9</sup>, Martin Eckstein<sup>4,10</sup>, and Daniele Fausti<sup>1,2,3,†</sup>

*1. Department of Physics, Università degli Studi di Trieste, Trieste, Italy.*

*2. Elettra Sincrotrone Trieste, Trieste, Italy.*

*3. Department of Physics, University of Erlangen-Nürnberg, Erlangen, Germany*

*4. Institute of Theoretical Physics, University of Hamburg, Hamburg, Germany*

*5. Dipartimento di Fisica, Politecnico di Milano, Milano, Italy*

*6. Department of Mechanical Engineering, Columbia University, New York, 10027, NY, USA*

*7. Department of Chemistry, Columbia University, New York, 10027, NY, USA*

*8. Department of Chemistry, Stanford University, Stanford, CA 94305, USA*

*9. Istituto di Fotonica e Nanotecnologie, Consiglio Nazionale delle Ricerche, Milano, Italy*

*10. The Hamburg Centre for Ultrafast Imaging, Hamburg, Germany*

\* These authors contributed equally to the work.

† Correspondence to: daniele.fausti@fau.de

## Abstract

Excitons in a monolayer transition metal dichalcogenide (1L-TMD) are highly bound states characterized by a Rydberg-like spectrum of discrete energy levels. Within this spectrum, states with odd-parity are known as dark excitons because transitions to the ground state are forbidden by selection rules. This makes their stationary and transient characterization challenging using linear optical techniques. Here, we demonstrate that the dynamics of a  $2p$  dark excitonic state in 1L-WS<sub>2</sub> can be directly retrieved by measuring the Autler-Townes splitting of bright states in a three-pulse experiment. The splitting of the bright  $1s$  excitonic state, observed by detuning a mid-infrared control field across the  $1s$ - $2p$  transition, provides an accurate characterization of the  $2p$  state, which is used here to reveal its dynamics following a sudden photoinjection of free carriers in the conduction band. We observe a qualitatively different dynamics of the  $1s$  and  $2p$  levels, which is indicative of symmetry-dependent screening and exciton-exciton interactions. These findings provide new insights into many-body effects in TMDs, offering potential avenues for advancing the next generation optoelectronics.

## Introduction

Monolayer transition metal dichalcogenides (1L-TMDs) are receiving increasing attention in recent years due to their unique electronic and optical properties which enable disruptive technological applications [1-3]. Their large nonlinear response [4,5] and rich excitonic photophysics [6,7] make them prime candidates for the development of innovative optoelectronic devices that leverage strong light-matter interactions. In these atomically thin semiconductors, the efficient coupling of excitonic states to light is a direct consequence of their reduced dimensionality and weak dielectric screening, which result in exceptionally high exciton binding energies [2]. This strong Coulomb interaction gives rise to a Rydberg-like spectrum of discrete excitonic energy levels, reminiscent of the energy levels of a hydrogen atom, but modified by the distinctive properties of the material's environment [8].

Within this spectrum, excitonic states are categorized as either "bright" or "dark" based on their ability to couple with light. While bright states (with even parity) strongly interact with photons and are easily observed in linear optical experiments, dark states (with odd parity) have a very weak optical response under normal conditions, making their characterization particularly challenging [9-11].

Recently, advanced spectroscopic tools or external perturbations (e.g., magnetic fields, strain, or nonlinear optical probes) have been used to break the optical selection rules [12-17] and access the dark excitonic landscape in different families of 1L-TMDs. In particular, the use of two-photon excitation

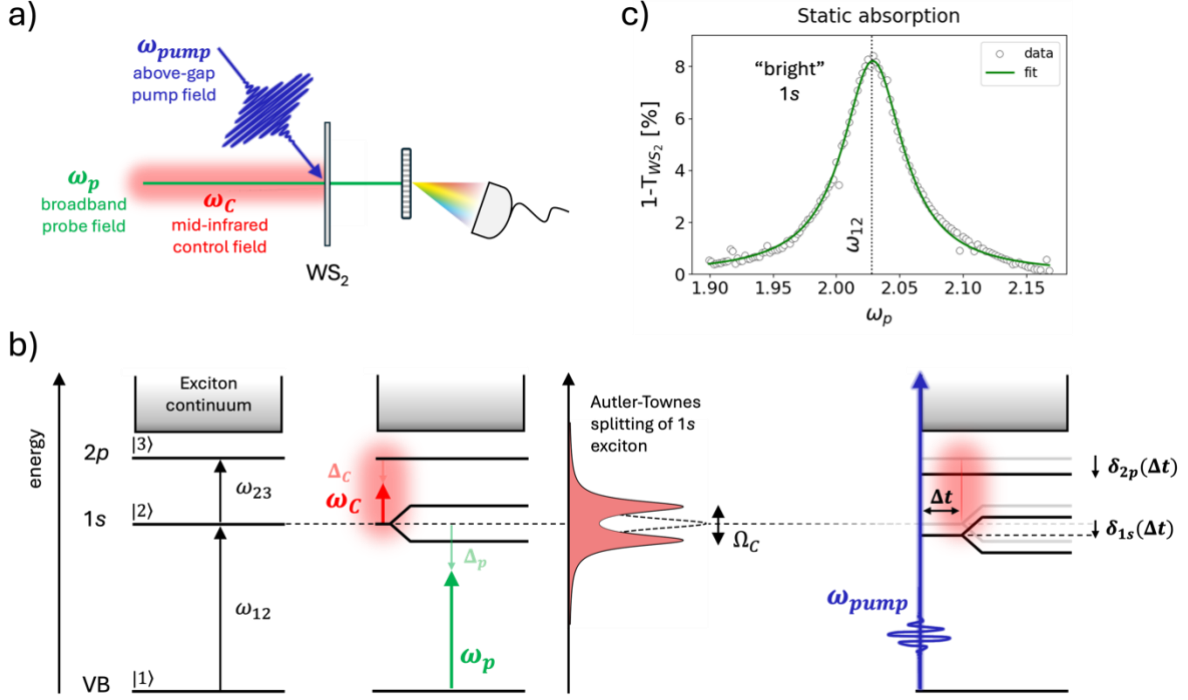


**Figure 1: Time-dependent Autler-Townes splitting to probe the dynamics of the 2p dark state.** a) Sketch of the experimental setup. b) Conceptualization of the experiment, in which the sample is modelled as an ensemble of 3-level systems. The excitation by a mid-infrared control field ( $\omega_c$ , red arrow) resonant to the 1s-2p transition ( $\omega_{23}$ ) triggers an Autler-Townes splitting of the bright 1s exciton, which is revealed by the broadband probe field ( $\omega_p$ , green arrow). The splitting is proportional to the Rabi frequency  $\Omega_c$  of the control field. A photoexcitation by an above-gap pump field ( $\omega_{pump} = 3.1$  eV, blue arrow) impulsively renormalizes the excitonic spectrum. The measurement of the Autler-Townes splitting as a function of time provides information on the pump-induced dynamics of the 2p dark state. c) Static absorption of 1L-WS<sub>2</sub> measured at equilibrium by means of the broadband probe field in the range 1.89-2.17 eV. The “bright” 1s state of the A exciton is fitted and found to lie at  $\omega_{12} = 2.029$  eV at room temperature.

spectroscopy has revealed a series of excitonic dark states in 1L-WS<sub>2</sub> that have been assigned to the odd-parity 2p and 3p levels of the A exciton [12]. These states exhibit remarkable robustness against variations in temperature and the dielectric environment (i.e., the capping) of the monolayer, suggesting that static perturbations do not alter the *p*-symmetry states.

However, the robustness of these dark states may not extend to impulsive perturbations. Several studies have shown that, upon photoexcitation, the early-time dynamics of the exciton population is dominated by processes such as phase space filling, bandgap renormalization and many-body exciton-exciton interactions [7, 18-22]. The simultaneous occurrence of these effects, each producing distinct and often opposing optical signatures, complicates the task of disentangling their respective contributions.

So far, experimental investigations have mainly focused on the non-equilibrium dynamics of bright excitons in 1L-TMDs. In this case, both experimental and theoretical studies suggest that the renormalization of the excitonic spectrum is dominated by the concurrent effects of the photoinduced shrinkage of the bandgap and the reduction of the exciton oscillator strength [18, 22, 23]. However, the ultrafast photoinduced dynamics of excitonic dark states is still largely unexplored. In particular, the strong spatial dependence of the screening induced by the photoinjected carriers and the subsequent establishment of exciton-exciton interactions could have a different impact on wavefunctions with different symmetries.

Here, we compare the dynamics of the 1s and 2p states of the A exciton in 1L-WS<sub>2</sub> following an impulsive above-gap photoexcitation at 3.1 eV ( $\omega_{pump}^1$  in Fig. 1a). To probe the 2p state, we develop

<sup>1</sup> We will always assume in the following that  $\hbar = 1$ .

a three-pulse technique that leverages the strong oscillator strength of the bright  $1s$  state to induce an Autler-Townes splitting in the optically active transition. This effect arises in the presence of a mid-infrared (mid-IR) control field ( $\omega_C$  in Fig. 1a) resonant with the  $1s$ - $2p$  transition. The transient transmissivity of the sample is then probed by a broadband visible pulse ( $\omega_p$  in Fig. 1a), whose spectrum covers the bright  $1s$  transition, which is dispersed and frequency-resolved after transmission.

The rationale of our approach is illustrated in Fig. 1b. The sample can be modelled as an ensemble of independent 3-level ladder systems, as depicted in the leftmost panel. The allowed optical transition between the  $1s$  exciton state ( $|2\rangle$ ) and the maximum of the valence band at the K point in the Brillouin zone ( $|1\rangle$ ) occurs at energy  $\omega_{12} = 2.029$  eV, while we indicate with  $\omega_{23}$  the energy separation between the  $2p$  ( $|3\rangle$ ) and the  $1s$  levels, which lies in the mid-IR range. The transition between  $|3\rangle$  and  $|1\rangle$  is instead dipole-forbidden, thus making  $|3\rangle$  a dark state.

When an intense pulsed control field  $\omega_C$  is applied and is tuned on resonance with the transition  $|2\rangle \rightarrow |3\rangle$ , a splitting of the transition into two “dressed” states occurs. This effect – which is the AC counterpart of the static Stark effect – is referred to as Autler-Townes splitting (ATS) [24] and arises from classical strong light-matter coupling. The modification of the eigenstates of the system can be probed by a second broadband field  $\omega_p$  which will detect a transparency in correspondence with level  $|2\rangle$  and the emergence of two new absorption peaks which are separated by the Rabi frequency  $\Omega_C = \mu_{23}E_C$ , where  $E_C$  is the amplitude of the strongly coupled field and  $\mu_{23}$  is the transition dipole moment of the  $|2\rangle \rightarrow |3\rangle$  transition.

It should be stressed that the framework we are discussing here is analogous to the one established in the context of light-driven atomic or molecular systems, in which the coherent preparation by a laser excitation leads to the well-known phenomenon of electromagnetically-induced transparency (EIT) [25, 26]. In our case, however, the intrinsic inhomogeneous broadening of the excitonic transitions and their fast dephasing times do not satisfy the conditions for EIT to occur, specifically  $\gamma_{13} < \gamma_{12}$ , where  $\gamma$  denotes the coherence decay rate of the states. Notably, our measurements reveal that the dephasing rate of the  $2p$  state is approximately three times higher than the one of the  $1s$  exciton, as it will be demonstrated below. This indicates that a coherent superposition cannot be sustained in the system under study, and destructive quantum interference does not occur.

Since the amplitude, the intensity and the central frequency of the ATS intrinsically depend on the spectral properties of level  $|3\rangle$  (i.e., its energy  $\omega_{23}$  and its coherence decay rate  $\gamma_{13}$ ), optical measurements of the ATS spectrum in our sample provide indirect insights on the dark  $2p$  state. This approach has previously been employed to resolve exciton fine structures in the K and K' valleys in MoSe<sub>2</sub> by coupling the  $1s$  and the  $2p^+$  and  $2p^-$  dark states using circularly polarized mid-IR pump pulses [27, 28]. In this work, we measure the ATS spectrum at varying time delays between the visible pump pulse and the mid-IR control field (rightmost panel in Fig. 1b). This allows us to achieve time-resolution and reconstruct the pump-induced dynamics of the  $2p$  state following the above-gap photoexcitation.

In order to formalize the experiment within an ATS framework, we developed a semi-classical model which couples a 3-level ladder system with both the mid-IR and the probe field (see Methods for details). The interaction Hamiltonian of the model is given by the Rabi interaction for each of the two allowed transitions:

$$H_{Rabi} = -\frac{\Omega_p}{2} (e^{-i(\omega_{12} + \Delta_p)t} |2\rangle\langle 1| + h.c.) - \frac{\Omega_C}{2} (e^{-i(\omega_{23} + \Delta_C)t} |3\rangle\langle 2| + h.c.) \quad [\text{Eq. 1}]$$

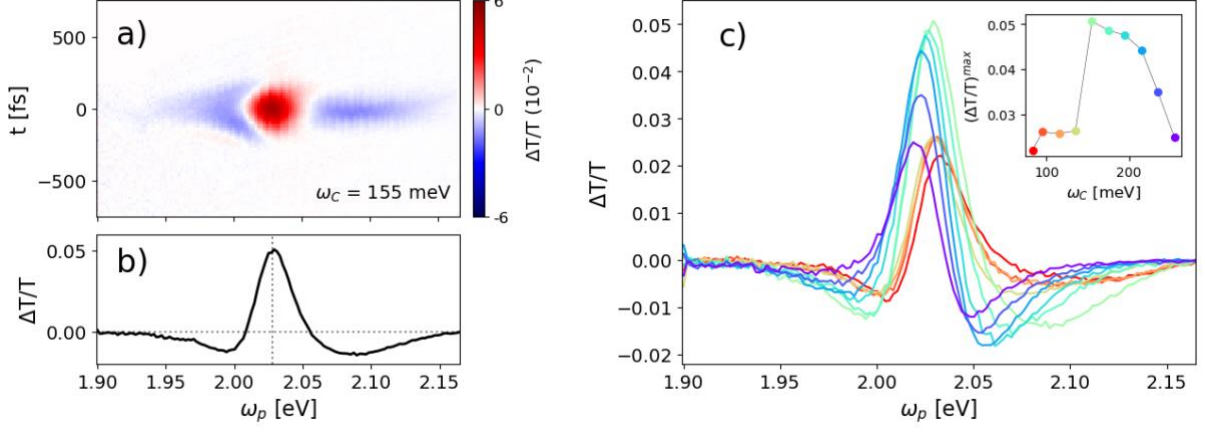


**Figure 2: Resonant Autler-Townes splitting in WS<sub>2</sub>.** a) Transient transmissivity map as a function of probe photon energy and delay between the mid-IR pump and the probe for a specific photon energy  $\omega_C = 155$  meV of the mid-IR control field. b) Transient spectrum at the temporal overlap. c) Spectra of the Autler-Townes splitting at the temporal overlap between the mid-IR pump and the probe for different photon energies of the pump. The inset shows the maximum  $\Delta T/T$  as a function of the mid-IR photon energy.

Where we have denoted by  $\Delta_p = \omega_p - \omega_{12}$  and  $\Delta_C = \omega_C - \omega_{23}$  the detunings of the probe and the control fields with respect to the excitonic transitions. We have also denoted by  $\Omega_p = \mu_{12}E_p$  the Rabi frequency of the probe field  $E_p$ , where  $\mu_{12}$  is the transition dipole moment of the  $|1\rangle \rightarrow |2\rangle$  transition. By computing the coherent evolution of the system within the density matrix formalism, we obtain an expression for the complex susceptibility for the transition from the ground state to the  $1s$  level, namely the transition monitored in our experiment as a function of the probe photon energy:

$$\chi(\Delta_p) = \frac{C}{\left| \frac{\Omega_C^2}{4} + (i\Delta_p + \gamma_{12})(i\Delta + \gamma_{13}) \right|^2} \left[ \left( \frac{\Omega_C^2}{4} \Delta - \Delta_1(\gamma_{13}^2 + \Delta^2) \right) + i \left( \frac{\Omega_C^2}{4} \gamma_{13} + \gamma_{12}(\gamma_{13}^2 + \Delta^2) \right) \right] \quad [\text{Eq. 2}]$$

where we have defined  $\Delta = \Delta_p + \Delta_C$ . Eq. 2 is a stationary solution of the equation of motion in the limit in which the probe field is much less intense than the mid-IR control field ( $\Omega_p/\Omega_C \ll 1$ ) and the excitonic states  $1s$  and  $2p$  are weakly populated. The susceptibility is proportional to the constant  $C = \frac{n|\mu_{12}|^2}{2\epsilon_0}$ , where  $n$  is the exciton density and  $\mu_{12}$  is the dipole moment of the  $1s$  transition.

It is important to stress that Eq. 2 has a general validity. Depending on the choice of the sample-specific parameters ( $C, \omega_{12}, \gamma_{12}$  and  $\gamma_{13}$ ) and the details of the control field ( $\Delta_C$  and  $\Omega_C$ , namely its photon energy and intensity), different coherent phenomena in any driven 3-level ladder system - ranging from ATS to EIT - can be described. A study of the parameter space of Eq. 2 is given in the Supplementary Note 1.

In order to consistently constrain the parameters in Eq. 2, we started by analyzing the static absorption of a large area 1L-WS<sub>2</sub> (Fig. 1c). The sample was obtained by gold-tape assisted exfoliation (see Methods for details) [29] and the absorption was measured at room temperature (see Supplementary Note 2). The  $1s$  excitonic peak features an absorption of  $\sim 8\%$  and has a Lorentzian shape centered at 2.029 eV, in agreement with previous studies [30]. The experimental curve has been fitted using the formula derived within the thin-film approximation in Ref. [20] and reported in Methods. We used the complex susceptibility in Eq. 2 in absence of the control field ( $\Omega_C = 0$ ) to constrain the remaining parameters related to the transition from the  $1s$  level to the ground state. The static absorption from  $1s$

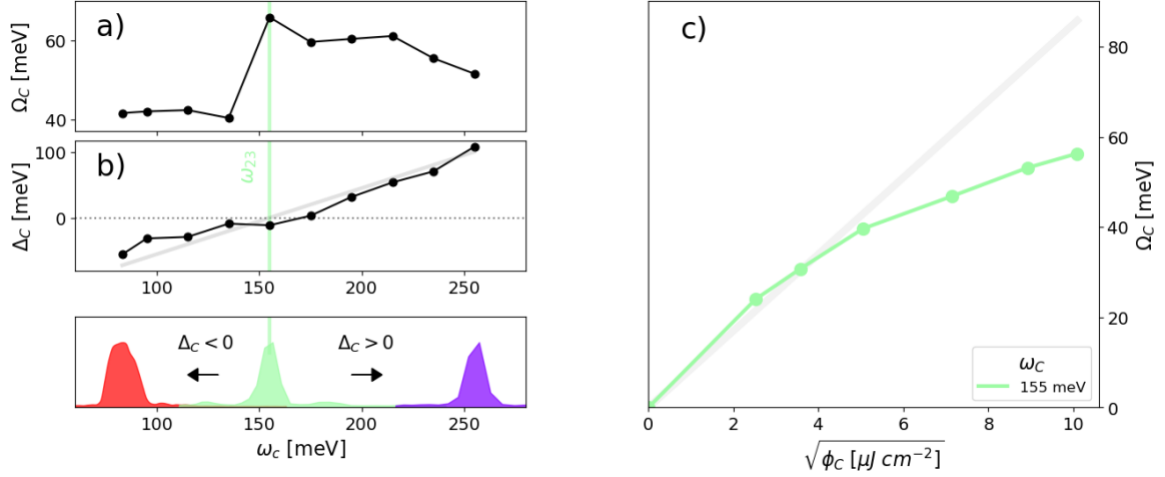


**Figure 3: Characterization of the dark 2p exciton.** a) Rabi frequency of the mid-IR control field as a function of its photon energy, as extrapolated from the fits. b) Extracted detuning of the mid-IR control field from the 1s-2p transition. The grey oblique line is the expected detuning considering  $\omega_{23} = 155$  meV. In the lower panel, three selected spectra of the mid-IR pulse measured by a home-made Michelson interferometer. c) Rabi frequency as a function of the square root of the mid-IR fluence for a resonant mid-IR pump ( $\omega_C = 155$  meV). The shadowed grey line follows the expected linear dependence.

exciton is found centered at  $\omega_{12} = 2.029$  eV and its width is  $\gamma_{12} = 21$  meV. Importantly, consistent values are obtained by fitting the absorption curve with a Lorentzian function, providing a valuable sanity-check for our model. Furthermore, the fitted value of the constant  $C$  provides an estimate for the dipole moment  $\mu_{12} = 45$  D, which agrees well with previous works [31].

Fig. 2 shows the transient differential transmissivity ( $\Delta T/T$ ) maps measured at room temperature upon excitation by the mid-IR field at photon energy  $\omega_C = 155$  meV. In this measurement, the above-gap pump is not used, and the goal is the characterization of the mid-IR induced ATS. The fluence of the mid-IR pump was set to  $50 \mu\text{J}/\text{cm}^2$ , while the fluence of the probe pulse was maintained to  $2 \mu\text{J}/\text{cm}^2$ . This justifies the approximation on the Rabi frequencies made in the model, i.e.,  $\Omega_p \ll \Omega_C$ . The color scale represents the pump-induced change in the probe transmissivity  $\Delta T/T$ , which in the perturbative limit corresponds to the opposite of the transient absorption  $\Delta A$ . This means that positive values in the maps (red) correspond to a decrease in the probe absorption. The vertical and the horizontal axes display the pump-probe time delay and the photon energy of the broadband probe, respectively. We observe a transient signal in proximity of the temporal overlap between the pump and the probe ( $t = 0$ ), which disappears within less than 500 fs. This short-lived signal confirms that the mid-IR pump pulse is acting as a gate field for the ATS to occur. In particular, an increased transmissivity is measured in correspondence with  $\omega_{12} = 2.029$  eV, confirming a suppressed absorption of the 1s excitonic state and the formation of doublets, appearing as blue regions of decreased transmissivity at both lower and higher energies with respect to  $\omega_{12}$ . This effect can be better visualized by plotting the  $\Delta T/T$  spectrum in Fig. 2b, where the vertical dotted line indicates the 1s absorption peak at equilibrium.

By varying the mid-IR photon energy and analyzing the corresponding  $\Delta T/T$  spectra at the pump-probe temporal overlap (Fig. 2c), the emergence of a resonance becomes evident. The amplitude of the transparency window reaches its maximum at  $\omega_C = 155$  meV (light green curve) and decreases for both higher and lower mid-IR pump photon energies, as shown in the inset of Fig. 2c. This reduction in amplitude is accompanied by a gradual shift of the transparency window toward higher probe photon energies as  $\omega_C$  decreases (from the purple to the red curve). The trend observed is consistent with our simulations with a varying detuning of the mid-IR field (Fig. S1d).

To quantitatively describe this behavior, a global fit of the curves in Fig. 2c was performed using Eq. 2. The fit function includes three free parameters:  $\Omega_C$ ,  $\Delta_C$ , and  $\gamma_{13}$ , with the constraint that  $\gamma_{13}$ , being an intrinsic material property, remains constant across all curves. Details of the fitting procedure and results are provided in the Supplementary Note 3. From the fit, we estimate  $\gamma_{13} = 65$  meV, corresponding to a dephasing rate of the 2p state that is approximately three times higher than that of the 1s state.

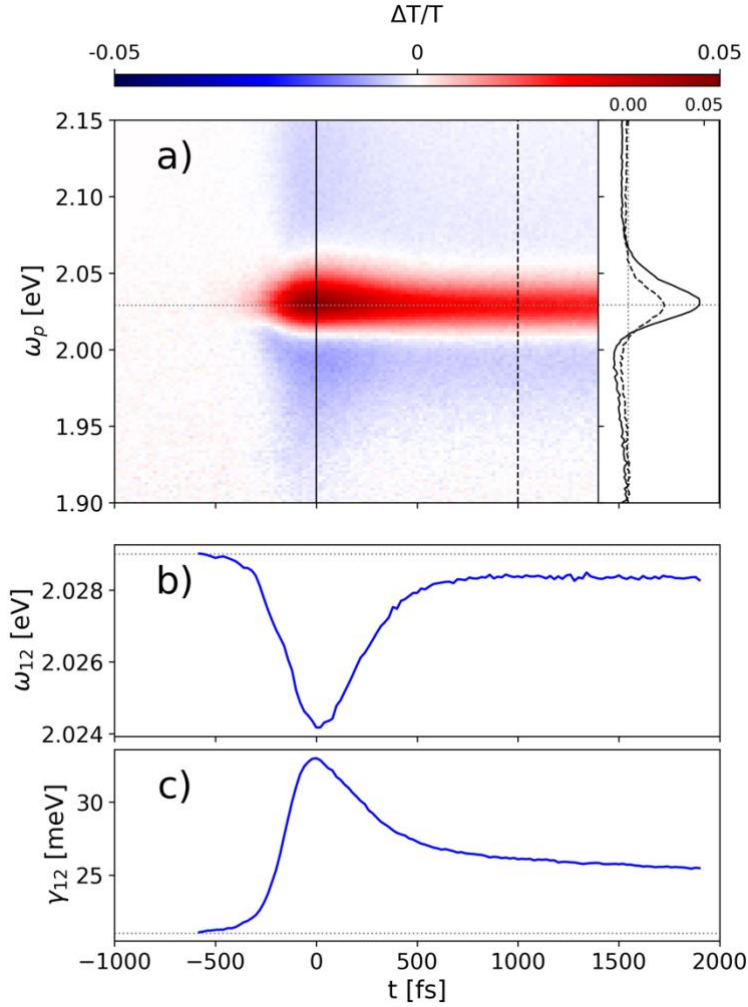


**Figure 4: Pump-induced dynamics of the bright 1s exciton.** a) Transient transmissivity map as function of probe photon energy and time delay, after a photoexcitation at  $\omega_{pump} = 3.1$  eV. The dotted horizontal line indicates the energy of the bright 1s exciton measured at equilibrium (Fig. 1c). The pump fluence is  $40 \mu\text{J}/\text{cm}^2$ . Inset: transient spectra (vertical cuts of the map) at  $t=0$  (solid line) and  $t=1$  ps (dashed line). d) Temporal evolution of the 1s exciton energy after photoexcitation, as extrapolated from the differential fit. e) Temporal evolution of the linewidth of the 1s exciton.

Fig. 3a and 3b present the extracted Rabi frequency and control field detuning, respectively, as functions of the incident mid-IR photon energy. In the lower panel of Fig. 3a and 3b, we plot three representative spectra of the mid-IR pulse measured through a home-made Michelson interferometer. The Rabi frequency (Fig. 3a) exhibits a maximum at  $\omega_C = 155$  meV, indicating that the coupling between the mid-IR control field and the  $|2\rangle \rightarrow |3\rangle$  transition is maximized under this condition. Similarly, the fitted detuning at this pump energy is  $\Delta_C = 0$  (Fig. 3b), implying that the control field is resonant with the  $1s-2p$  energy separation at a driving photon energy of 155 meV. This provides a precise estimate of the intraexcitonic  $1s-2p$  transition energy. We emphasize that the fitted value of  $\Delta_C$  is consistent with the expected detuning, given  $\omega_{23} = 155$  meV (indicated by the shaded grey line in Fig. 3b). This agreement serves as a critical validation of the model and the fitting procedure, ensuring their reliability and accuracy.

Our estimated value for the  $1s-2p$  energy separation is approximately 80 meV smaller than that reported in Ref. [12], which was determined using two-photon excitation spectroscopy. We reckon that this discrepancy may originate from differences in the experimental methodologies employed. In Ref. [12], the authors derived the energy separation by measuring photoluminescence as a function of the two-photon energy required to excite the  $2p$  state. In contrast, our approach involves direct measurement of the absorption between the  $1s$  and  $2p$  energy levels. Notably, the  $1s-2p$  energy separation obtained in our study coincides with the onset of the  $2p$  photoluminescence peak observed in the two-photon excitation spectroscopy measurements reported in Ref. [12].

We investigated the transiently induced ATS under a resonant mid-IR driving across a range of pumping fluences (see Supplementary Note 3 for the complete dataset and corresponding fits). Fig. 3c presents the extracted Rabi frequency as a function of the square root of the incident mid-IR fluence ( $\sqrt{\phi_C}$ ). As expected, the Rabi frequency initially follows a linear dependence on  $\sqrt{\phi_C}$  (grey line), reflecting its

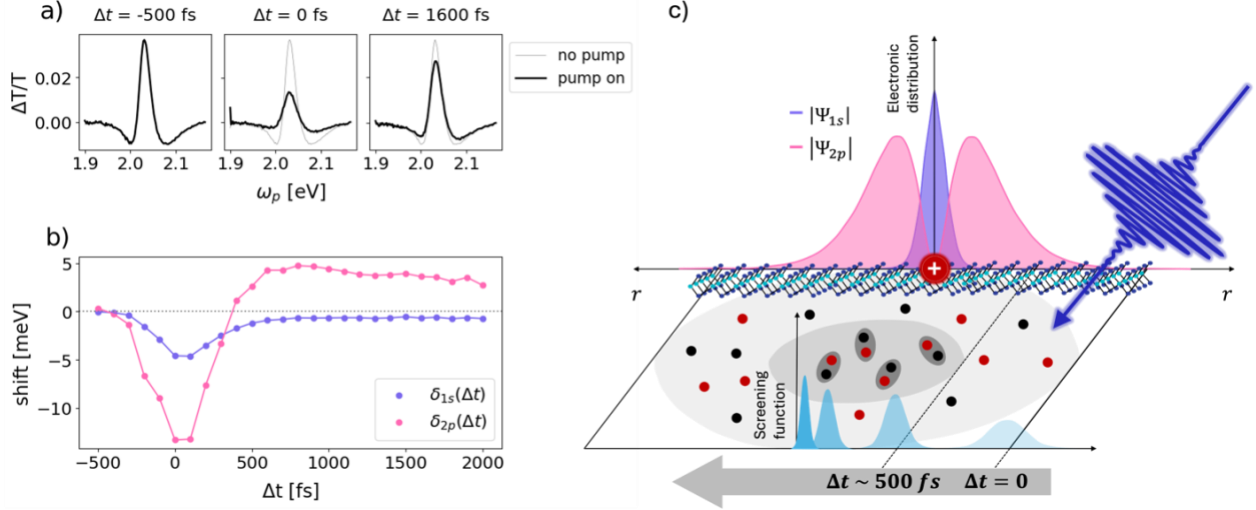


**Figure 5: Ultrafast screening of Rydberg-like excitonic levels.** *a)* Resonant ( $\omega_c = 155$  meV) Autler-Townes splitting with (black) and without (grey) the photoexcitation by the above-gap pump. Three selected time-delays between the visible and the mid-IR pump are reported. *b)* Transient renormalization of the 1s (purple) and the 2p (pink) excitonic levels upon photoexcitation by the visible pump ( $\omega_{pump} = 3.1$  eV). *c)* Conceptual schematization of the ultrafast screening of excitons with *s*- and *p*-symmetry wavefunctions, where *r* indicates the exciton radius, i.e., the separation between a positively-charged hole (red circle at the origin of the axes) and a negatively-charged electron. In the plane, the effects of an above-gap pulsed excitation are sketched: *i)* a sudden photoinjection of free charges at  $t = 0$ ; *ii)* the formation at later times of new bound excitons. The screening, which is mostly delocalized right after the photoexcitation, becomes more and more localized as exciton-exciton interactions start to be established.

direct proportionality to the field amplitude. Notably, at higher fluences,  $\Omega_C$  approaches a saturation value. This saturated behavior is also evident in the measured ATS amplitude (Fig. S7). This saturation may originate from a Pauli blocking mechanism initiated by the resonant driving. It is interesting to note that this saturation is not observed when the mid-IR field is detuned from the  $1s$ - $2p$  resonance (Fig. S9). In this case, either for a positive or a negative detuning, a linear dependence on  $\sqrt{\phi_C}$  is observed also at higher fluences.

The characterization of the mid-IR-induced ATS as a function of pump photon energy and fluence provides a strong validation of our model. The fitting results allow us to extract the control field detuning relative to the  $|2\rangle \rightarrow |3\rangle$  transition, enabling an accurate estimation of the  $1s$ - $2p$  energy separation.

Thus far, our analysis assumes an initial equilibrium state before interaction with the control field, using static parameters of the  $1s$  transition from equilibrium absorption. However, studying the photoinduced dynamics of the  $2p$  state requires understanding the  $1s$  exciton's response to photoexcitation. Since the  $1s$  energy and linewidth dynamically evolve under above-gap pumping, a full characterization is necessary to benchmark ATS at each time delay. As our model predicts only relative shifts between the  $1s$  and  $2p$  levels, the precise knowledge of the absolute  $1s$  transition energy is crucial for quantifying the  $2p$  renormalization.

Fig. 4a shows the  $\Delta T/T$  map measured upon photoexcitation by an above-gap pump at  $\omega_{pump} = 3.1$  eV. At the temporal overlap, the signal presents a second-derivative-like profile centered at the energy of the  $1s$  exciton at equilibrium, denoted by the dotted horizontal line. At later times ( $t > 500$  fs), the signal exhibits a derivative-like shape, displaying a negative shoulder at lower energies.  $\Delta T/T$  spectra at  $t = 0$  and  $t = 1$  ps are plotted in the inset as solid and dashed lines, respectively.

In order to translate the  $\Delta T/T$  map into an evolution of the excitonic peak, we performed a differential fit based on the absorption spectrum measured at equilibrium (Fig. 1c). For each time delay, we fitted the transient absorption spectrum, as detailed in Supplementary Note 5. The time evolution of the fitting parameters  $\omega_{12}$  and  $\gamma_{12}$  is plotted in Fig. 4b and 4c, respectively.

Upon photoexcitation, the  $1s$  peak undergoes two major modifications: a redshift of its central energy by  $\sim 5$  meV and a broadening of its lineshape. Both these effects occur in a time window of less than 1 ps. At longer pump-probe delays, a longer dynamics – associated to interactions with the lattice [32] – persists up to at least  $t = 25$  ps (Fig. S12). All these results are consistent with previous measurements in the same compound and similar 1L-TMDs [18, 20, 22].

We used the temporal evolution of  $\omega_{12}$  and  $\gamma_{12}$  to benchmark the time-resolved ATS experiment. The experimental setting is the one sketched in the rightmost panel of Fig. 1b: after the photoexcitation by  $\omega_{pump}$  renormalizes the excitonic spectrum, the mid-IR pump and the broadband probe impinge in sequence on the sample at varying time delay  $\Delta t$  with respect to the first perturbation. Details regarding the differential acquisition required for the three-pulse measurements are provided in Supplementary Note 7. In Fig. 5a, we present three representative ATS spectra, comparing the cases in the absence (grey) and presence (black) of an above-gap pump photoexciting the sample. The three panels correspond to distinct time delays  $\Delta t$  between the pump and mid-IR excitation: for  $\Delta t < 0$ , the mid-IR pulse precedes the visible pump, while for  $\Delta t > 0$ , the mid-IR pulse follows the visible pump. In the panels, we plotted only the  $\Delta T/T$  spectra taken when the probe is in temporal overlap with the mid-IR pulse. The full 2D maps are displayed in Fig. S13. The measurements in Fig. 5a indicate that the visible photoexcitation, which exerts its strongest influence at the temporal overlap between the two pumps ( $\Delta t = 0$ , central panel), induces a quenching and a broadening of the ATS transparency window.

We densely scanned the time delay between the two pumps (see Supplementary Note 7 for the full set of data). For each time delay, we fitted the ATS spectra similarly to what we did for the spectra in Fig. 3a but using the time-dependent parameters for the  $1s$  transition.

We found that the fitting parameter of the ATS that is mostly affected by the photoexcitation is  $\Delta_C$ , meaning that the relative distance between the  $1s$  and the  $2p$  level is dynamically modulated by the above-gap photoexcitation. By considering the evolution extracted for  $\omega_{12}$  (Fig. 4b), we can disentangle the pump-induced dynamics of the  $2p$  level only. We compare in Fig. 5b the pump-induced shift of both the  $1s$  level [ $\delta_{1s}(\Delta t)$ , purple curve, as already shown in Fig. 4b] and the  $2p$  one [ $\delta_{2p}(\Delta t)$ , pink curve]. We observe that also the  $2p$  state experiences a pump-induced redshift, whose amplitude at early times is more than twice the one of the  $1s$  state. Furthermore, the dynamics of  $\delta_{2p}(\Delta t)$  is faster and, within 500 fs, the  $2p$  level blueshifts by about 5 meV.

We propose a tentative explanation for this observation by considering the influence of spatially dependent ultrafast screening on wavefunctions with different symmetry and different principal quantum number [33]. Figure 5c summarizes the temporal evolution of screening and exciton-exciton interactions following photoexcitation. At early time delays, the primary effect of above-gap photoexcitation is the injection of free charge carriers into the system. Initially, these carriers are homogeneously distributed, leading to enhanced effective screening for excitonic states with larger spatial separation between the electron and hole. Consequently, states with higher principal quantum numbers experience more significant renormalization. This accounts for the dynamics observed in Fig. 5b, where the energy shift of the  $2p$  state is more than twice that of the  $1s$  state.

At later time delays, additional effects become relevant. Following photoexcitation, free carriers form strongly bound excitons. The calculated excitation density of the above-gap photoexcitation is  $1.2 \times 10^{13} \text{ cm}^{-2}$  and, if compared to previous works [20], this estimate suggests that the renormalization mechanism is no longer dominated by screening from free charges but also involves exciton-exciton interactions. As excitons localize, the screening function becomes spatially inhomogeneous within the plane, affecting wavefunctions with different spatial distributions in distinct ways.

Conventionally, exciton-exciton interactions in 1L-TMDs are described within a semiclassical framework, treating excitons as neutral particles with finite polarizability that experience long-range dipole-dipole repulsion [34, 35], which results in a net blueshift of the excitonic energies. Recent theoretical work [35] further demonstrates that a blueshift can also arise from the fermionic nature of the exciton substructure, analogous to Pauli blocking of the fermionic phase space. This effect leads to a "hardcore" exciton-exciton repulsion, contributing to an increase in excitonic energies.

The observed time-dependent blueshift of the  $2p$  level suggests that one or both of these repulsive exciton-exciton interactions become significant as free carriers bind into excitons. The absence of a



similar blueshift in the  $1s$  state may be attributed to the spatial extent of the wavefunctions. Specifically, the  $2p$  exciton, being more spatially extended, is more susceptible to phase-space filling and repulsive interactions in a high-density exciton regime, whereas the more localized  $1s$  state is less affected.

In conclusion, we have introduced a novel methodology to probe dark states in 1L-TMDs. The unique strength of our approach lies in the addition of time resolution, that has not been previously achievable using other nonlinear techniques. This allowed us to temporally track the energy shift of the  $2p$  dark state in 1L-WS<sub>2</sub> in response to above-gap photoexcitation. The comparison of its dynamics with that of the bright  $1s$  exciton enabled us to disentangle the dominant screening mechanisms at different time scales following the photoexcitation and, especially, to single out the contribution of exciton-exciton interactions to the renormalization of the dark state. Access to the dynamics of dark excitons may provide more insights into the relaxation pathways of bright excitons and their influence on light-matter interactions in this class of materials, with significant implications for optoelectronics applications, including photodetectors, light-emitting devices, and valleytronics. Finally, we stress that the presented approach is not restricted to the study of dark  $p$ -symmetry states in 1L-TMDs but can be extended to other systems and energy levels, provided that the oscillator strengths of the states involved are sufficiently high.

## Methods

### 1. Sample preparation

Monolayers WS<sub>2</sub> are mechanically exfoliated from a bulk WS<sub>2</sub> single crystal (HQ Graphene) using a gold-tape exfoliation technique previously reported in Ref. [29]. The process begins by depositing a gold layer onto a clean Si wafer, followed by spin-coating with a polyvinylpyrrolidone (PVP) polymer layer. The PVP/Au stack is then lifted from the Si wafer using thermal release tape (Nitto) and brought into contact with a freshly cleaved WS<sub>2</sub> bulk crystal, exfoliating a large WS<sub>2</sub> monolayer. The tape/PVP/Au/WS<sub>2</sub> stack is then transferred onto a double-side-polished fused silica substrate. The thermal release tape is removed by heating to 100°C, and the PVP layer is eliminated through water rinsing and O<sub>2</sub> plasma treatment. Finally, the gold layer is dissolved using a KI/I<sub>2</sub> etchant solution (KI 99.9%, I<sub>2</sub> 99.99%, Alfa Aesar) in deionized water. After thorough rinsing with water and isopropanol, a clean WS<sub>2</sub> monolayer is obtained on the fused silica substrate.

### 2. Experimental setup

The source of the experimental apparatus was a regeneratively amplified Yb-KGW laser (Pharos, Light Conversion), which delivers 290 fs pulses at 1.2 eV with an average power of 20 W. The laser operated at a repetition rate of 10 kHz. The sample was excited by tunable mid-IR pulses (ranging from 83 to 255 meV) generated by difference frequency mixing in a GaSe crystal, from two near-infrared beams produced in a Twin Optical Parametric Amplifier (Orpheus TWIN by Light Conversion). A homemade Michelson interferometer, equipped with a mercury cadmium telluride detector, was used to measure the wavelength of the mid-IR pulses. A 3.1 eV pump pulse was obtained through second harmonic generation in a  $\beta$ -barium borate crystal, using the output from a Non-Collinear Parametric Amplifier (Orpheus-N by Light Conversion). Both pumps were mechanically modulated by two synchronized optical choppers running at 45 and 90 Hz. More details about the experimental apparatus are given Ref. [36].

The transmissivity of the sample under non-equilibrium conditions was probed using a broadband pulse covering 1.3 eV to 2.2 eV, obtained by white-light continuum generation of the Pharos laser output in a 6-mm-thick sapphire crystal. Prior to interaction with the sample, the probe was filtered using a bandpass filter (1.9–2.16 eV) to center its spectral window on the  $1s$  bright exciton peak. When focused on the sample, the mid-IR pump, the blue pump and the probe beams have Gaussian spot sizes with FWHM of  $\sim 100 \mu\text{m}$ ,  $\sim 100 \mu\text{m}$  and  $\sim 30 \mu\text{m}$ , respectively. All three pulses were linearly polarized.

The transmitted probe beam was diffracted by a transmission grating (1200 grooves/mm), and its spectral components were detected by a linear array of silicon photodiodes (NMOS by Hamamatsu), synchronized with the laser's repetition rate. To improve the signal-to-noise ratio, a reference beam (not interacting with the sample) was simultaneously measured and used to normalize the data, reducing fluctuations in the white-light probe. While no physical adjustments were made to correct for the temporal chirp of the broadband probe, all data were processed after acquisition to account for dispersion effects.

All the measurements discussed in the manuscript have been performed at room temperature.

### 3. Theoretical model

The system has been described as an ensemble of independent 3-level systems, following the approach in Ref. [26].

Contrarily to Ref. [26], we used a ladder-type 3-level-system instead of a lambda-type – namely, the forbidden transition in our case is the one from the lowest energy level to the highest energy one, instead of that from lowest to intermediate.

The exciton dynamics has been described by the master equation in the interaction picture:

$$\dot{\rho} = -\frac{i}{\hbar}[H_0 + H_{Rabi}(t), \rho] + \mathcal{D}[\rho] \quad [\text{Eq. 3}]$$

where  $H_0$  is the unperturbed Hamiltonian of the 3-level-system

$$H_0 = \omega_1 \sigma_{11} + \omega_2 \sigma_{22}$$

with  $\sigma_{ij} = |i\rangle\langle j|$ , while  $H_{Rabi}$  is the time-dependent Rabi Hamiltonian in Eq. 2, where the Rabi frequencies are defined as

$$\Omega_p = |\vec{\mu}_{12}^* \cdot \vec{E}_p|, \quad \Omega_C = |\vec{\mu}_{23}^* \cdot \vec{E}_C|,$$

with  $\mu_{ij}$  being the dipole matrix element of the transition between the states  $|i\rangle$  and  $|j\rangle$ , and  $\vec{E}_p, \vec{E}_C$  the electric field amplitudes of the probe and control pulses. Moreover, the dissipator operator  $\mathcal{D}$  describes decay processes from higher- to lower-energy levels and the dephasing of the off-diagonal density matrix elements; it is defined as

$$\begin{aligned} \mathcal{D}[\rho] = & \frac{\Gamma_{31}}{2} (2\sigma_{12}\rho\sigma_{21} - \{\sigma_{22}, \rho\}) + \frac{\Gamma_{32}}{2} (2\sigma_{23}\rho\sigma_{32} - \{\sigma_{33}, \rho\}) + \frac{\gamma_{2d}}{2} (2\sigma_{22}\rho\sigma_{22} - \{\sigma_{22}, \rho\}) \\ & + \frac{\gamma_{3d}}{2} (2\sigma_{33}\rho\sigma_{33} - \{\sigma_{33}, \rho\}). \end{aligned}$$

The coefficients  $\Gamma_{31}$ ,  $\Gamma_{32}$ ,  $\gamma_{2d}$  and  $\gamma_{3d}$  are phenomenological: the former two respectively quantify the decay rate from  $|2\rangle$  to  $|1\rangle$  and from  $|3\rangle$  to  $|2\rangle$ ; whereas the latter two respectively describe the dephasing processes of the level  $|2\rangle$  and  $|3\rangle$ , which effectively reduce the coherence of the system. Notice that the presence of the dephasing terms is critical for tuning the linear optical susceptibility to the right shape and eventually provides the knob to tune the amplitude of the transparency window (see Supplementary Note 1 for further details).

Let now  $\rho_{ij} = \langle i|\rho|j\rangle$ ,  $i, j = 1, 2, 3$  be the generic matrix element of the density matrix. The values of the diagonal terms  $\rho_{11}$ ,  $\rho_{22}$ ,  $\rho_{33}$  reflect the populations of the states  $|1\rangle$ ,  $|2\rangle$ ,  $|3\rangle$ . For the off-diagonal terms one can switch to a rotating frame by setting

$$\begin{aligned} \rho_{12} &= r_{12} e^{i\omega_p t}, \\ \rho_{23} &= r_{23} e^{i\omega_C t}, \\ \rho_{13} &= r_{13} e^{i(\omega_p + \omega_C) t}. \end{aligned}$$

The Bloch equations then follow from the master equation in Eq. 3:

$$\begin{aligned}
\dot{\rho}_{11} &= -\frac{i}{2}(\Omega_p r_{12} - \Omega_p^* r_{12}^*) + \Gamma_{12} \rho_{22}; \\
\dot{\rho}_{22} &= \frac{i}{2}(\Omega_p r_{12} - \Omega_p^* r_{12}^*) - \frac{i}{2}(\Omega_c r_{23} - \Omega_c^* r_{23}^*) - \Gamma_{21} \rho_{22} + \Gamma_{32} \rho_{33}; \\
\dot{\rho}_{33} &= \frac{i}{2}(\Omega_c r_{23} - \Omega_c^* r_{23}^*) - \Gamma_{32} \rho_{33}; \\
\dot{r}_{12} &= \frac{i}{2} \Omega_p^* (\rho_{22} - \rho_{11}) - \frac{i}{2} \Omega_c r_{13} - (i\Delta_p + \gamma_{12}) r_{12}; \\
\dot{r}_{13} &= -\frac{i}{2} \Omega_c^* r_{12} + \frac{i}{2} \Omega_p^* r_{23} - (i(\Delta_p + \Delta_c) + \gamma_{13}) r_{13}; \\
\dot{r}_{23} &= \frac{i}{2} \Omega_p r_{13} + \frac{i}{2} \Omega_c^* (\rho_{33} - \rho_{22}) - (i\Delta_c + \gamma_{23}) r_{23}.
\end{aligned}$$

The new decay rates have been introduced

$$\gamma_{12} = \frac{1}{2}(\Gamma_{21} + \gamma_{2d}), \quad \gamma_{13} = \frac{1}{2}(\Gamma_{32} + \gamma_{3d}), \quad \gamma_{23} = \gamma_{12} + \gamma_{23},$$

respectively quantifying the lifetime of the off-diagonal matrix elements  $r_{ij}$ .

The term  $r_{12}$  in particular is needed for computing the contribution to the optical susceptibility of the transition  $|1\rangle$ - $|2\rangle$ , which is the one measured in the experiment:

$$\chi(\Delta_p, \Delta_c) = C \frac{r_{12}^*(\Delta_p, \Delta_c)}{\Omega_p}$$

[Eq. 4]

where

$$C = \frac{n\mu_{12}^2}{\epsilon_0}.$$

The quantity  $n$  is an effective density of excitons per unit volume, while  $\mu_{12}$  is the dipole moment of the transition. The former can be thought of as the density of available excitonic states of the systems, while the actual population of the states  $|i\rangle$  will be given by  $n\rho_{ii}$ .

The equilibrium value of  $\chi$  is determined by solving the equations of motion for  $r_{12}$  in the stationary case, namely when  $\dot{r}_{ij} = 0 \forall i, j$ . It is reasonable to assume that the intensity of the probe field is much smaller than that of the control field, therefore that the Rabi frequencies would satisfy

$$\lambda = |\Omega_p|/|\Omega_c| \ll 1;$$

Furthermore, this implies that the states  $|2\rangle$  and  $|3\rangle$  have negligible population, thus one can also assume that  $\rho_{11} \approx 1$ , while  $\rho_{22} \approx \rho_{33} \approx 0$ .

With such approximations, in the stationary regime one finds the following linear system for the coefficients  $r_{ij}$ :

$$\begin{pmatrix}
-(i\Delta_p + \gamma_{12}) & -i\Omega_c / 2 & 0 \\
-i\Omega_c / 2 & -[i(\Delta_p + \Delta_c) + \gamma_{13}] & i\Omega_p / 2 \\
0 & i\Omega_p / 2 & -(i\Delta_c + \gamma_{23})
\end{pmatrix}
\begin{pmatrix}
r_{12} \\
r_{13} \\
r_{23}
\end{pmatrix}
=
\begin{pmatrix}
i\Omega_p^* / 2 \\
0 \\
0
\end{pmatrix},$$

which can then be solved in perturbation theory to first order in  $\lambda$ . Inserting the value of  $r_{12}$  into the expression for  $\chi$  of Eq. 4 finally leads to the formula of susceptibility (Eq. 2 in the main text).

Finally, the transmission has been worked out within the thin-film approximation. The approximation considers the current density in 1L-WS<sub>2</sub> to have a delta-like profile and takes into account the influence of the semi-infinite (500µm thick) dielectric substrate of fused silica [20]. By solving the Maxwell's equations with the appropriate boundary conditions, it is possible to obtain an expression for the transmittance of the monolayer:

$$T(\omega_p) = \frac{4n_{sub}}{\left(1 + n_{sub} + \frac{\omega_p d}{c} \Im(\chi)\right)^2 + \left(\frac{\omega_p d}{c} \Re(\chi)\right)^2} \quad [\text{Eq. 5}]$$

where  $n_{sub}$  is refractive index of the substrate ( $n_{sub} = 1.458$  for fused silica at 2 eV) and  $d$  is the thickness of the monolayer ( $d = 0.67 \text{ nm}$  for 1L-WS<sub>2</sub>). Eq. 5 has been used to fit the experimental data.

## References

1. Koppens, F., Mueller, T., Avouris, P. et al. Photodetectors based on graphene, other two-dimensional materials and hybrid systems. *Nature Nanotech* **9**, 780–793 (2014).
2. Wang, G. et al. *Colloquium*: Excitons in atomically thin transition metal dichalcogenides. *Rev. Mod. Phys.* **90**, 021001 (2018).
3. Mueller, T., Malic, E. Exciton physics and device application of two-dimensional transition metal dichalcogenide semiconductors. *npj 2D Mater Appl* **2**, 29 (2018).
4. Autere, A. et al. Nonlinear Optics with 2D Layered Materials. *Advanced Materials* **30**, 24 (2018).
5. Trovatello, C., Marini, A., Xu, X. et al. Optical parametric amplification by monolayer transition metal dichalcogenides. *Nat. Photonics* **15**, 6–10 (2021).
6. Moody, G., Schaibley, J. & Xu, X. Exciton dynamics in monolayer transition metal dichalcogenides. *J. Opt. Soc. Am. B* **33**, C39-C49 (2016).
7. Dal Conte, S. et al. Ultrafast Photophysics of 2D Semiconductors and Related Heterostructures. *Trends in Chemistry* **2**, 1 (2020).
8. Chernikov, A. et al. Exciton Binding Energy and Nonhydrogenic Rydberg Series in Monolayer WS<sub>2</sub>. *Phys. Rev. Lett.* **113**, 076802 (2014).
9. Berghäuser, G., Knorr, A. & Malic, E. Optical fingerprint of dark 2p-states in transition metal dichalcogenides. *2D Mater.* **4** 015029 (2017).
10. Malic, E. et al. Dark excitons in transition metal dichalcogenides. *Phys. Rev. Materials* **2**, 014002 (2018).
11. Brem, S., Selig, M., Berghaeuser, G. et al. Exciton Relaxation Cascade in two-dimensional Transition Metal Dichalcogenides. *Sci Rep* **8**, 8238 (2018).
12. Ye, Z., Cao, T., O'Brien, K. et al. Probing excitonic dark states in single-layer tungsten disulphide. *Nature* **513**, 214–218 (2014).
13. Wang, G. et al. Giant Enhancement of the Optical Second-Harmonic Emission of WSe<sub>2</sub> Monolayers by Laser Excitation at Exciton Resonances. *Phys. Rev. Lett.* **114**, 097403 (2015).
14. Cha, S., Sung, J., Sim, S. et al. 1s-intraexcitonic dynamics in monolayer MoS<sub>2</sub> probed by ultrafast mid-infrared spectroscopy. *Nat Commun* **7**, 10768 (2016).
15. Berghäuser, G. et al. Mapping of the dark exciton landscape in transition metal dichalcogenides. *Phys. Rev. B* **98**, 020301(R) (2018).
16. He, M., Cai, J., Zheng, H. et al. Dynamically tunable moiré exciton Rydberg states in a monolayer semiconductor on twisted bilayer graphene. *Nat. Mater.* **23**, 224–229 (2024).
17. Quian, C. et al. Probing Dark Excitons in Monolayer MoS<sub>2</sub> by Nonlinear Two-Photon Spectroscopy. *Phys. Rev. Lett.* **133**, 086902 (2024).

18. Pogna, E. et al. Photo-Induced Bandgap Renormalization Governs the Ultrafast Response of Single-Layer MoS<sub>2</sub>. *ACS Nano* **10**, 1, 1182–1188 (2016).
19. Cunningham, P. et al. Photoinduced Bandgap Renormalization and Exciton Binding Energy Reduction in WS<sub>2</sub>. *ACS Nano* **11**, 12, 12601–12608 (2017).
20. Sie, E. et al. Observation of Exciton Redshift–Blueshift Crossover in Monolayer WS<sub>2</sub>. *Nano Lett.* **17**, 7, 4210–4216 (2017).
21. Trovatiello, C., Katsch, F., Borys, N.J. et al. The ultrafast onset of exciton formation in 2D semiconductors. *Nat Commun* **11**, 5277 (2020).
22. Trovatiello, C. et al. Disentangling Many-Body Effects in the Coherent Optical Response of 2D Semiconductors. *Nano Lett.* **22**, 13, 5322–5329 (2022).
23. Chernikov, A., Ruppert, C., Hill, H. et al. Population inversion and giant bandgap renormalization in atomically thin WS<sub>2</sub> layers. *Nature Photon* **9**, 466–470 (2015).
24. Autler, S. & Townes, C. Stark Effect in Rapidly Varying Fields. *Phys. Rev.* **100**, 703 (1955).
25. Harris, S., Field, J. & Imamoğlu, A. Nonlinear optical processes using electromagnetically induced transparency. *Phys. Rev. Lett.* **64**, 1107 (1990).
26. Fleischhauer, M., Imamoğlu, A. & Marangos, J. Electromagnetically induced transparency: Optics in coherent media. *Rev. Mod. Phys.* **77**, 633 (2005).
27. Yong, C.K., Utama, M.I.B., Ong, C.S. et al. Valley-dependent exciton fine structure and Autler–Townes doublets from Berry phases in monolayer MoSe<sub>2</sub>. *Nat. Mater.* **18**, 1065–1070 (2019).
28. Slobodeniuk, A.O., Koutenský, P., Bartoš, M. et al. Ultrafast valley-selective coherent optical manipulation with excitons in WSe<sub>2</sub> and MoS<sub>2</sub> monolayers. *npj 2D Mater Appl* **7**, 17 (2023).
29. Liu, F. et al. Disassembling 2D van der Waals crystals into macroscopic monolayers and reassembling into artificial lattices. *Science* **367**, 903–906 (2020).
30. Zhu, B., Chen, X. & Cui, X. Exciton Binding Energy of Monolayer WS<sub>2</sub>. *Sci Rep* **5**, 9218 (2015).
31. Wu, Q. et al. Strong coupling of excitons in monolayer WS<sub>2</sub> with guided-mode resonance. *Results in Physics* **44**, 106191 (2023).
32. Ruppert, C. et al. The Role of Electronic and Phononic Excitation in the Optical Response of Monolayer WS<sub>2</sub> after Ultrafast Excitation. *Nano Lett.* **17**, 2, 644–651 (2017).
33. Aßmann, M. & Bayer, M. Semiconductor Rydberg Physics. *Adv. Quantum Technol.* **3**, 11, 1900134 (2020).
34. Xiao, K. et al. Exciton–Exciton Interaction in Monolayer MoSe<sub>2</sub> from Mutual Screening of Coulomb Binding. *ACS Nano* **18**, 46, 31869–31876 (2024).
35. Steinhoff, A. et al. Exciton-Exciton Interactions in Van der Waals Heterobilayers. *Phys. Rev. X* **14**, 031025 (2024).
36. Montanaro, A. et al. Visible pump–mid infrared pump–broadband probe: Development and characterization of a three-pulse setup for single-shot ultrafast spectroscopy at 50 kHz. *Rev. Sci. Instrum.* **91**, 073106 (2020).

## Acknowledgements

The authors acknowledge insightful discussions with Atac Imamoğlu. This work was mainly supported by the European Research Council through the project INCEPT (grant agreement no. 677488). D.F., A.M., F.F., G.J. and E.M.R. acknowledge the support of the Gordon and Betty Moore Foundation through the grant (CENTQC). Monolayer sample preparation was supported by the Materials Science and Engineering Research Center (MRSEC) through NSF grant DMR-2011738 (XYZ). C.T. and G.C. acknowledge the European Union’s Horizon Europe research and innovation program under the Marie Skłodowska-Curie PIONEER HORIZON-MSCA-2021-PF-GF (grant agreement no. 101066108). M.E. and F.V. were supported by the Cluster of Excellence “CUI: Advanced Imaging of Matter“ of the Deutsche Forschungsgemeinschaft (DFG) – EXC 2056 – project ID 390715994.

## **SUPPLEMENTARY MATERIALS**

# Supplementary Note 1: Simulations

We discuss here some features of the 3-level model outlined in the main text.

Firstly, we point out that the expression obtained for  $\chi$  (Eq. 2) predicts electromagnetically induced transparency (EIT), namely the opening of a narrow transparency window in the absorption spectrum, when the following conditions are satisfied:

$$\gamma_{12} \gg |\Omega_c| \gg \sqrt{\gamma_{12}\gamma_{13}}.$$

The rate  $\gamma_{12}$  provides then a natural energy scale to which compare other energy quantities.

Let us first consider the case  $\gamma_{13} = 0$ , namely when there is not any additional dephasing. In this situation, the transparency is perfect, meaning that the imaginary part of the susceptibility is exactly zero at zero probe detuning ( $\Delta_p = 0$ ). This is clear in the light blue curve in Fig. S1a. However, when the Rabi frequency of the control field  $\Omega_c$  is increased towards values comparable to or higher than  $\gamma_{12}$ , the shape of the susceptibility changes qualitatively: instead of a sharp and narrow transparency window, a line splitting occurs.

A finite dephasing  $\gamma_{13} \neq 0$  quenches the transparency, as it is illustrated in Fig. S1b. As  $\gamma_{13}$  increases at a fixed control field amplitude, the imaginary part of the susceptibility at zero probe detuning takes a finite value and it is completely canceled out when  $\gamma_{13} > \gamma_{12}$ . In the Autler-Townes regime (Fig. S1c) – i.e., for more intense control fields – the splitting is also smeared out by increasing  $\gamma_{13}$ .

Finally, in Fig. S1d the effect of the detuning of the control field is highlighted. The choice of parameters  $\gamma_{13}$  and  $\Omega_c$  is such that the system is in the EIT regime, but we highlight that a similar trend is present also in the Autler-Townes regime. The detuning shifts the position of the transparency window, making the susceptibility profile asymmetric.

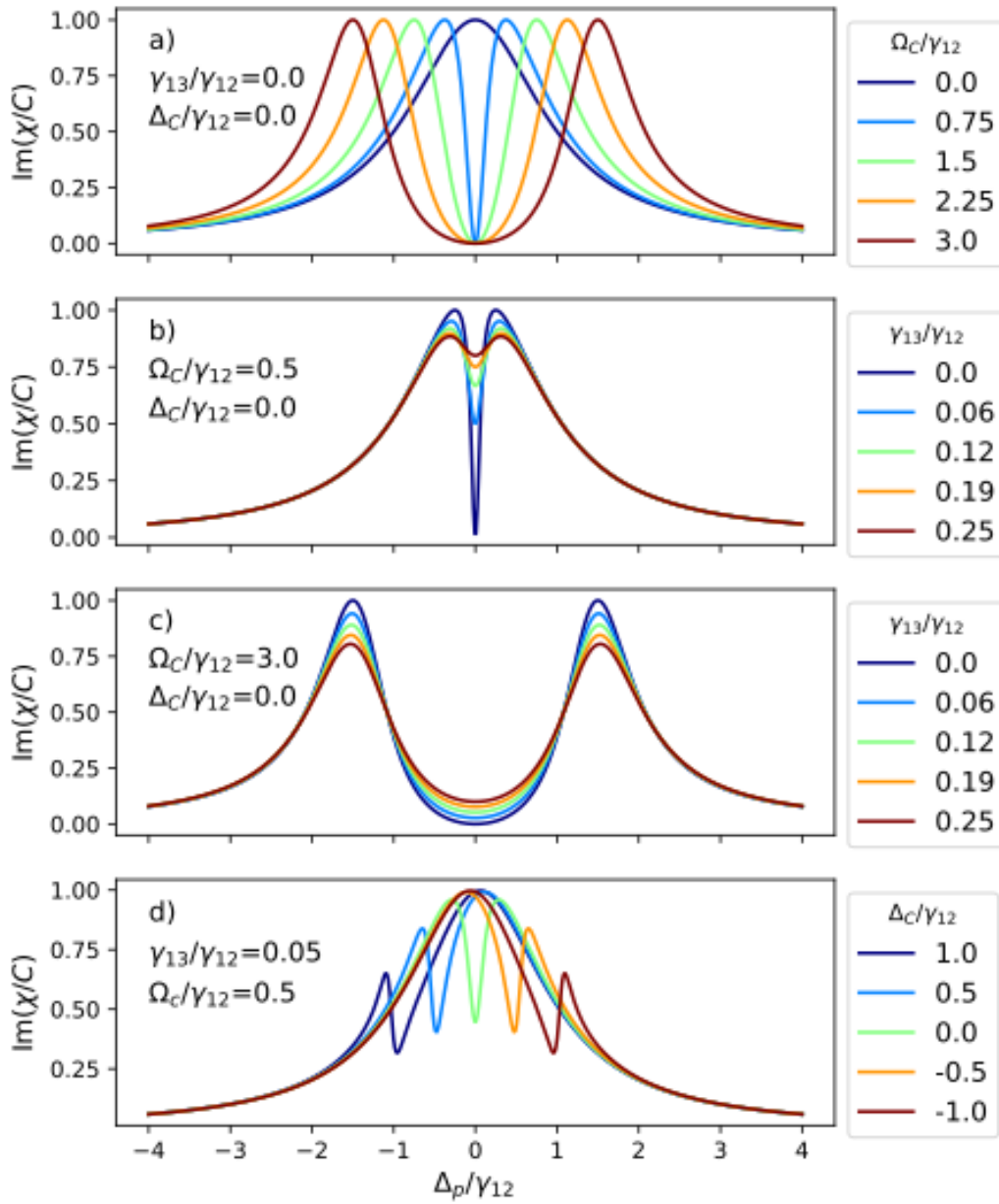


Figure S4: **Imaginary part of linear susceptibility as a function of different parameters** a) Dependence of the susceptibility on the Rabi frequency of the control field. At low values of  $\Omega_C$  ( $0.25\gamma_{12}$ ,  $0.5\gamma_{12}$ ) the transparency window is very narrow, indicating that EIT occurs; as the Rabi frequency is increased, a splitting of the absorption spectrum takes place. b) Effect of dephasing coefficient  $\gamma_{13}$  in the EIT regime and in c) in the Autler-Townes one. d) Effect of finite pump detuning (notice that since  $\gamma_{13}$  is finite the EIT is not perfect).



## Supplementary Note 2: Analysis of the static absorption

The static absorption of the sample has been measured at room temperature using the same broadband probe employed in the time-resolved experiments.

Three different spectra have been acquired:

- i. the dark spectrum of the photodiode array ( $S_{bkg}$ ).
- ii. the spectrum transmitted by the fused silica substrate ( $S_{sub}$ ).
- iii. the spectrum transmitted by the sample ( $S_{sam}$ ).

In Fig. S2a we plot the spectra transmitted by the substrate (grey) and the sample (black) after subtracting the background. We observe an overall decrease of the amount of light transmitted by the sample, and in particular a dip at around 2 eV. This reduced transmission corresponds to the absorption by the bright 1s exciton.

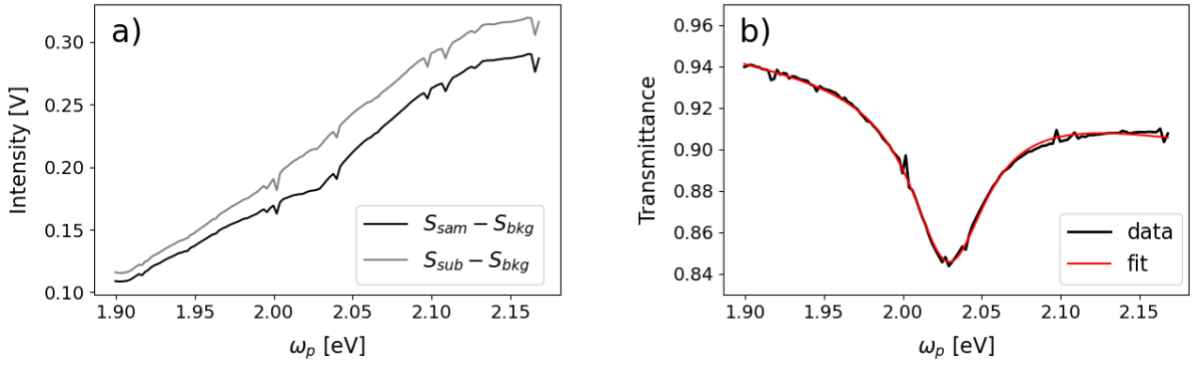


Figure S2: a) Spectra transmitted by the substrate (grey) and the sample (black) at equilibrium. b) Transmittance of the sample fitted using Eq. S2 and considering the expression for the equilibrium susceptibility (Eq. S1).

We plot in Fig. S2b the transmittance of the sample ( $T$ ), obtained as ratio between the curves in Fig. S2a. The transmittance displays a Lorentzian shape superimposed to a linear background. In the absorption plotted in Fig. 1c, the linear background has been subtracted.

To fit the data, we used the model developed for the complex susceptibility (Eq. 2 in the main text) in the limit in which the system is at equilibrium – i.e., no mid-infrared control field is applied. In this condition, Eq. 2 can be rearranged considering that  $\Omega_c = 0$ . By separating the real and imaginary part, we obtain:

$$\begin{cases} \Re[\chi_{eq}(\omega_p)] = -C \frac{\omega_p - \omega_{12}}{(\omega_p - \omega_{12})^2 + \gamma_{12}^2} \\ \Im[\chi_{eq}(\omega_p)] = +C \frac{\gamma_{12}}{(\omega_p - \omega_{12})^2 + \gamma_{12}^2} \end{cases}$$

[Eq. S1]

The transmittance at equilibrium has been then fitted by Eq. 5 (in Methods section) using the equilibrium susceptibility in Eq. S1. The fitting function has therefore five free parameters:  $C$ ,  $\omega_{12}$ ,  $\gamma_{12}$  and two remaining parameters for the linear background. As discussed in the main text,  $C = 0.455$  eV,  $\omega_{12} = 2.029$  eV and  $\gamma_{12} = 21$  meV.

# Supplementary Note 3: Fits of the induced Autler-Townes splitting

## i. As a function of mid-infrared detuning

To study dependence of the Autler-Townes splitting on the detuning of the control field, we changed the mid-IR photon energy in the range 83-255 meV and we measured the transient transmissivity. The fluence was kept constant and equal to  $50 \mu\text{J}/\text{cm}^{-2}$  throughout the measurements.

The maps in Fig. S3 show time- and energy-resolved  $\Delta T/T$  maps measured. The map acquired at  $\omega_C = 155$  meV is the one reported in Fig. 2a and corresponds to the resonance with the 1s-2p transition ( $\Delta_C = 0$ ). In this case, as discussed in the main text, the transparency window at the temporal overlap ( $t = 0$ ) features a symmetric shape across the energy axis with a negative-positive-negative profile. When the mid-IR photon energy is decreased to the minimum value ( $\omega_C = 83$  meV,  $\Delta_C < 0$ ), the transparency has a reduced intensity and an asymmetric shape, with a more pronounced negative shoulder at lower probe energies. The asymmetry is reversed for the highest mid-IR photon energy measured ( $\omega_C = 255$  meV,  $\Delta_C > 0$ ).

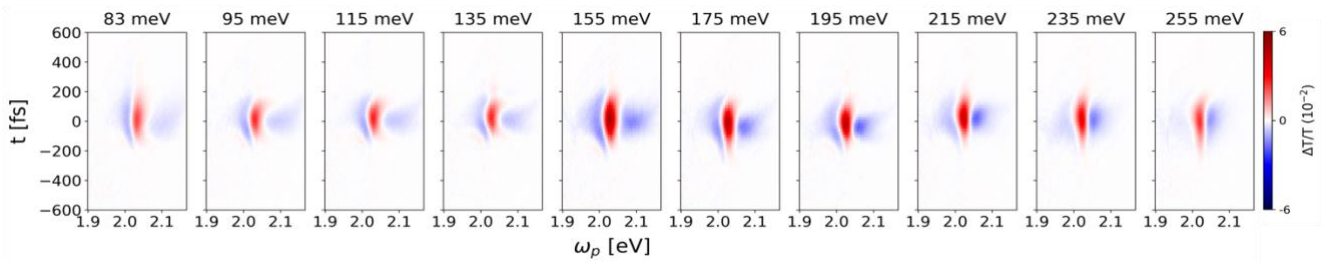


Figure S3: Time- and energy-resolved  $\Delta T/T$  maps upon interaction with mid-infrared fields of varying photon energy.

This trend is even clearer in Fig. S4, where the black dots show horizontal cuts of the maps in Fig. S3 at the temporal overlap. All the curves have been globally fitted using the following expression:

$$\frac{\Delta T}{T} = \frac{T(\omega_p) - T(\omega_p, \Omega_C = 0)}{T(\omega_p, \Omega_C = 0)}$$

[Eq. S2]

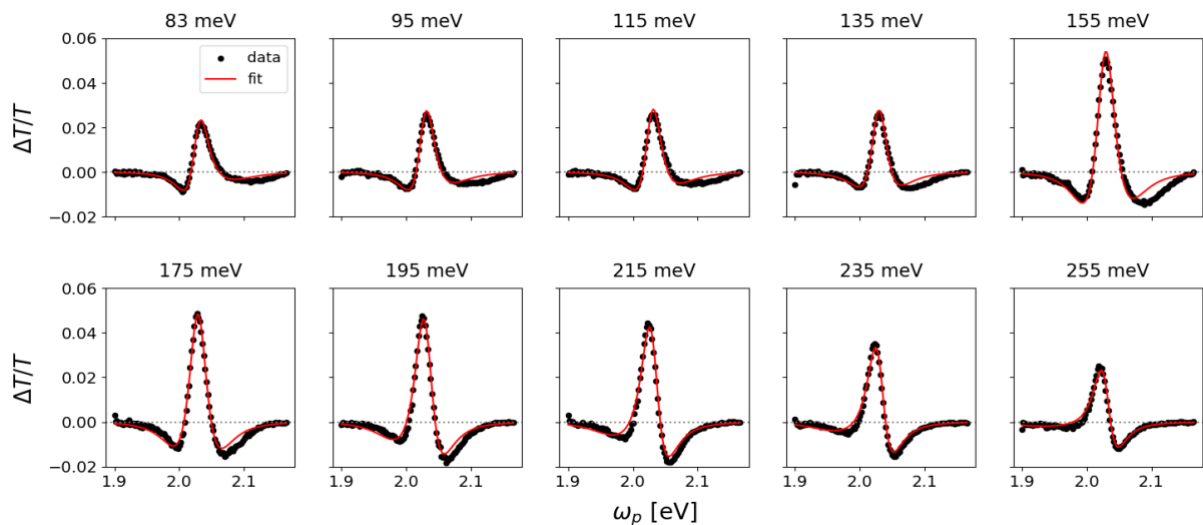


Figure S4: Spectra (black dots) at the temporal overlap taken from the maps in Fig. S3 and corresponding fits (red lines).

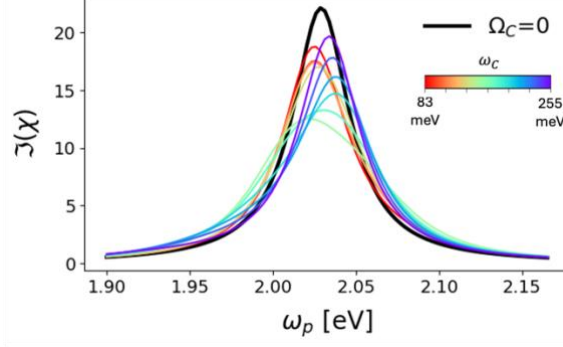


Figure S5: Imaginary part of the susceptibility calculated in the absence of the mid-infrared field ( $\Omega_C = 0$ ) and upon interaction with a mid-infrared field having the parameters obtained by fitting the experimental curves in Fig. S4.

where  $T(\omega_p)$  is Eq. 5 in Methods accounting for the transmission when the mid-IR control field impinges on the sample and  $T(\omega_p, \Omega_C = 0)$  is again Eq. 5 but with a null Rabi frequency, that is including the equilibrium susceptibility (Eq. S1).

The global fitting procedure has been carried out using the *lmfit* routine in Python. The expression of  $T(\omega_p)$  has five parameters:  $C$ ,  $\omega_{12}$ ,  $\Omega_C$ ,  $\Delta_C$ ,  $\gamma_{12}$  and  $\gamma_{13}$ . Among these,  $C$ ,  $\omega_{12}$  and  $\gamma_{12}$  are fixed parameters and their values are constrained by the equilibrium measurements (Supplementary Note 2). Furthermore, being  $\gamma_{13}$  a material-dependent property, it should be the same across all the measurements performed by detuning the mid-IR control field. We therefore constrained the global fit in such a way that  $\gamma_{13}$  is a free fitting parameter but it should have the same value for all the curves in Fig. S4. The parameters  $\Omega_C$  and  $\Delta_C$  are instead free to change. The results of the global fit are plotted as red lines superimposed to the data in Fig. S4.

As discussed in the main text, the best global fit is obtained for  $\gamma_{13} = 65$  meV.  $\Omega_C$  and  $\Delta_C$  extracted from the fit are instead plotted as a function of the mid-IR photon energy in Fig. 2a and 2b, respectively. In particular, the dependence of  $\Delta_C$  on  $\omega_C$  constitutes a “sanity-check” for the model: as expected, the  $\Delta_C = 0$  condition is obtained for  $\omega_C = 155$  meV. Both the negative and positive detunings are correctly retrieved.

In order to study how the 1s absorption is modified by the interaction with the mid-IR control field, we plot in Fig. S5 the imaginary part of the susceptibility in Eq. 2. For each colored curve in Fig. S5, we included in the calculation the fitting parameters obtained by the global fits of the curves in Fig. S4. The black line is instead the equilibrium absorption in the absence of the mid-IR field ( $\Omega_C = 0$ ). The plot indicates that the strongest quench of the absorption is observed at  $\omega_C = 155$  meV (light green curve). However, a more pronounced splitting of the Autler-Townes doublet (like the one simulated in Fig. S1a) is never achieved within the parameter space explored in the experiment.

## ii. As a function of mid-infrared fluence

The dependence of the Autler-Townes splitting on the control field intensity has been studied by keeping fixed the photon energy of the mid-IR field on resonance with the 1s-2p transition ( $\omega_C = 155$  meV) and changing its fluence.

Fig. S6 shows the transient  $\Delta T/T$  maps for the set of fluences measured. The spectra at the temporal overlap are plotted in Fig. S7 (black dotted curves). We fitted the spectra following the same approach discussed in the previous paragraph. In this case, the only parameter let free to change for every curve was  $\Omega_C$ . The parameters  $\Delta_C$  and  $\gamma_{13}$  have been instead constrained so that they have the same value across the dataset. The optimal fit has been achieved for  $\Delta_C = 14$  meV and  $\gamma_{13} = 65$  meV. The slightly positive detuning obtained is visible in the red fitting curves in Fig. S7, which feature an asymmetric shape especially at higher fluences. The decay rate  $\gamma_{13}$  is then consistent with the one found in the previous set. The Rabi frequency extracted is plotted in Fig. 3c of the main text as a function of the mid-IR fluence. The imaginary part of the susceptibility calculated for each fluence is plotted in Fig. S7. A complete splitting of the doublet is not observed even at the highest fluence measured.

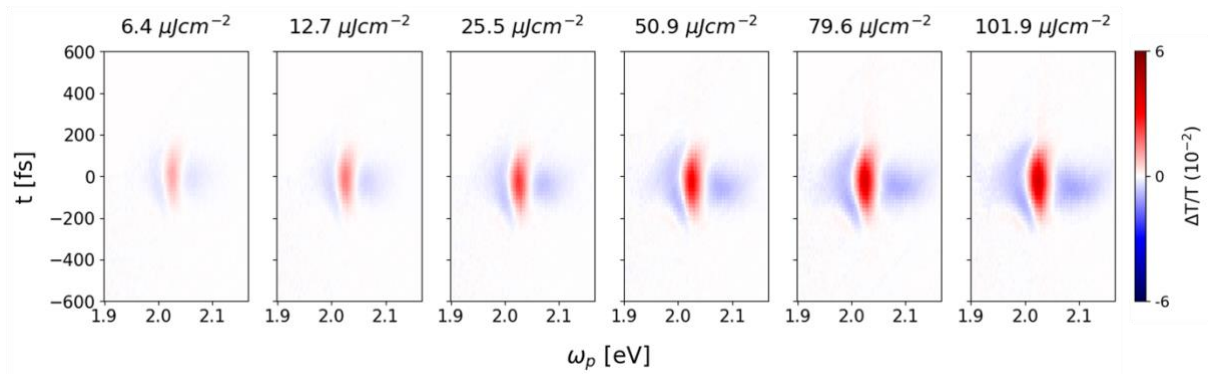


Figure S6: Time- and energy-resolved  $\Delta T/T$  maps upon interaction with mid-infrared fields of varying fluence at constant photon energy ( $\omega_c = 155$  meV).

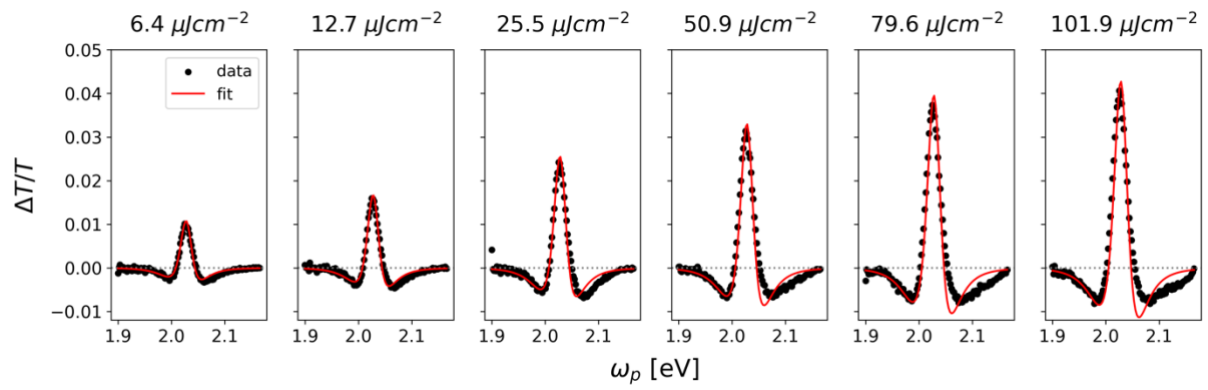


Figure S7: Spectra (black dots) at the temporal overlap taken from the maps in Fig. S6 and corresponding fits (red lines).

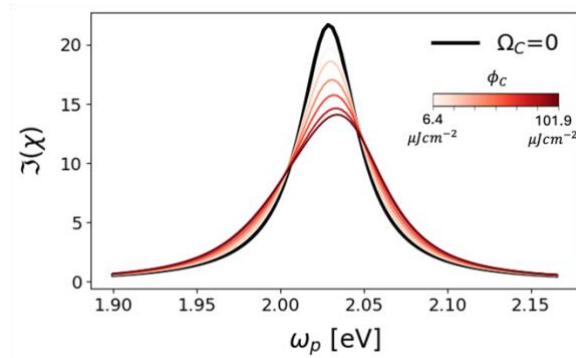


Figure S8: Imaginary part of the susceptibility calculated in the absence of the mid-infrared field ( $\Omega_C = 0$ , black line) and upon interaction with a mid-infrared field with the parameters obtained by fitting the experimental curves in Fig. S7.

## Supplementary Note 4: Fluence dependence for detuned mid-IR driving

We measured the transient  $\Delta T/T$  maps as a function of fluence (as in Fig. S6) for other two selected photon energies of the mid-IR control field,  $\omega_C = 83$  meV and  $\omega_C = 275$  meV. These two energies correspond to a negative and a positive detuning, respectively. The fluence-dependent curves have been fitted following the same procedure described in the previous section. The two independent sets have been globally fitted with the constraint that  $\gamma_{13}$  is the same for all curves and that  $\Delta_C$  is the same for all the fluence-dependent curves within the same set. The extrapolated value of  $\gamma_{13}$  was again 65 meV, confirming the robustness of the fitting procedure. We retrieved a value of  $\Delta_C = -44$  meV and  $\Delta_C = 124$  meV for the negative and positive detuning, respectively.

In Fig. S9 we plot the Rabi frequencies extrapolated from the fits as a function of the square root of the mid-IR fluence for both sets. The shadowed grey lines follow a linear dependence and are a guide for the eye. Both curves are compatible with a linear trend and do not display saturation at higher fluences. This is consistent with the expected trend of the Rabi frequency of the mid-IR pulse which should linearly scale with the amplitude of the field. The saturated behavior observed at  $\omega_C = 155$  meV (Fig. 3c) is thus peculiar of an excitation by a resonant field.

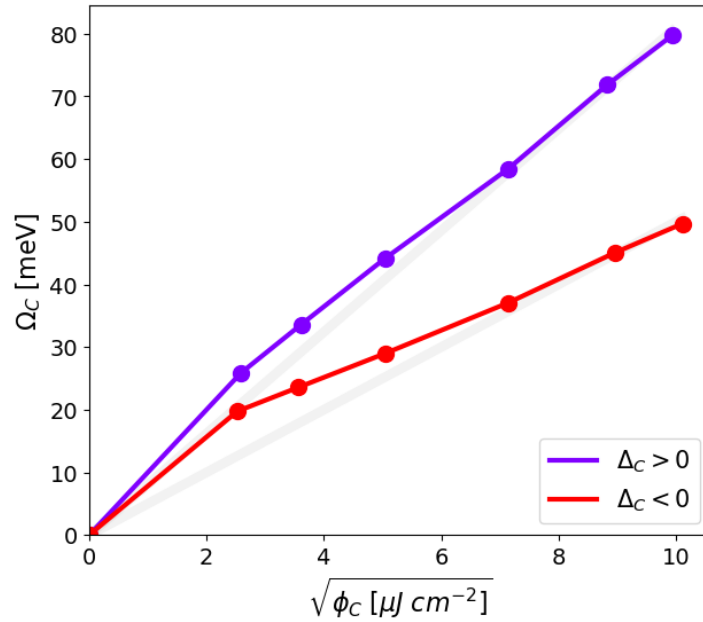


Figure S9: Rabi frequency as a function of the square root of the mid-IR fluence for a positively- (purple,  $\omega_C = 275$  meV) and a negatively-detuned (red,  $\omega_C = 83$  meV) mid-IR pump as extrapolated from the global fits.

## Supplementary Note 5: Fit of the above-gap pump-induced dynamics

The transient  $\Delta T/T$  map in Fig. 4 has been measured upon photoexcitation by a pump pulse ( $\omega_{pump} = 3.1$  eV) at fluence  $40 \mu\text{J cm}^{-2}$ .

To extract the temporal evolution of the central frequency ( $\omega_{12}$ ) and the width ( $\gamma_{12}$ ) of the 1s transition, we performed a differential fit at every time delay measured. The black dotted curves in Fig. S10 are representative  $\Delta T/T$  spectra at selected times. The fit function used is:

$$\frac{\Delta T}{T} = \frac{T^{exc}(\omega_p, \Omega_C = 0) - T(\omega_p, \Omega_C = 0)}{T(\omega_p, \Omega_C = 0)}$$

Where  $T(\omega_p, \Omega_C = 0)$  is the transmittance in Eq. 5 in Methods evaluated at equilibrium (static absorption fit in Fig. S2b), while  $T^{exc}(\omega_p, \Omega_C = 0)$  has the same functional form but the parameters  $C$ ,  $\omega_{12}$  and  $\gamma_{12}$  are let free to vary. We find that the parameter  $C$  does not significantly influence the fit, as the optimal values for the central frequency and the width of the transition remain unchanged whether  $C$  is held constant or allowed to vary freely. The corresponding fits are overlaid as red lines in Fig. S10, while the temporal evolution of the parameters  $\omega_{12}$  and  $\gamma_{12}$  is plotted in Figs. 4d and 4e, respectively.

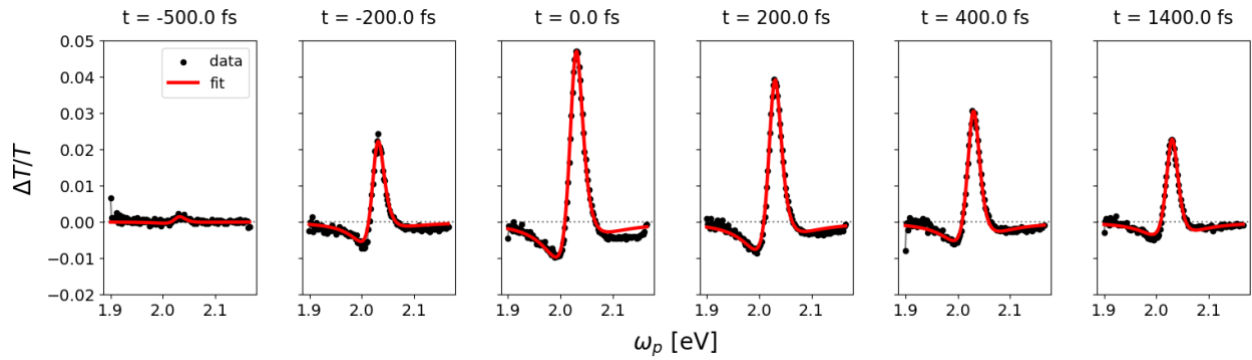


Figure S10:  $\Delta T/T$  spectra at selected time delays between the visible pump and the broadband probe (black dots) and corresponding fits (red lines).

In Fig. S11, we present the calculated transmittance based on the out-of-equilibrium parameters derived from the fitting procedure for several representative time delays. The black curve corresponds to the equilibrium transmittance prior to photoexcitation. The results demonstrate that the most significant perturbation occurs at temporal overlap ( $t = 0$ , dark blue line), and it is characterized by a redshift and a broadening of the absorption peak. As the time delay increases (light blue curve), the out-of-equilibrium transmittance gradually converges toward the static condition.

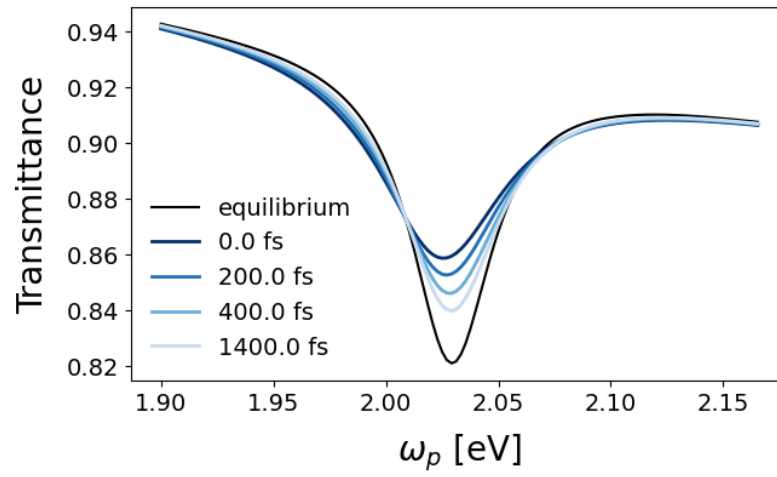


Figure S11: Calculated transmittance of 1L-WS<sub>2</sub> using the parameters obtained by the time-dependent fits. The black curve is the fitted equilibrium transmission (red line in Fig. S2b).

## Supplementary Note 6: Long-time dynamics of the 1s exciton

We plot in Fig. S12 the transient  $\Delta T/T$  of 1L-WS<sub>2</sub> measured upon photoexcitation by a pump pulse ( $\omega_{pump} = 3.1$  eV) at fluence  $20 \mu J cm^{-2}$ . The pump-induced changes to the transmissivity exhibit a long-lived response, reaching a plateau that remains visible at late time delays ( $t = 25$  ps). This dynamics has been observed to persist over hundreds of picoseconds and is primarily dominated by interactions with the lattice, mediated by exciton-phonon scattering [32].

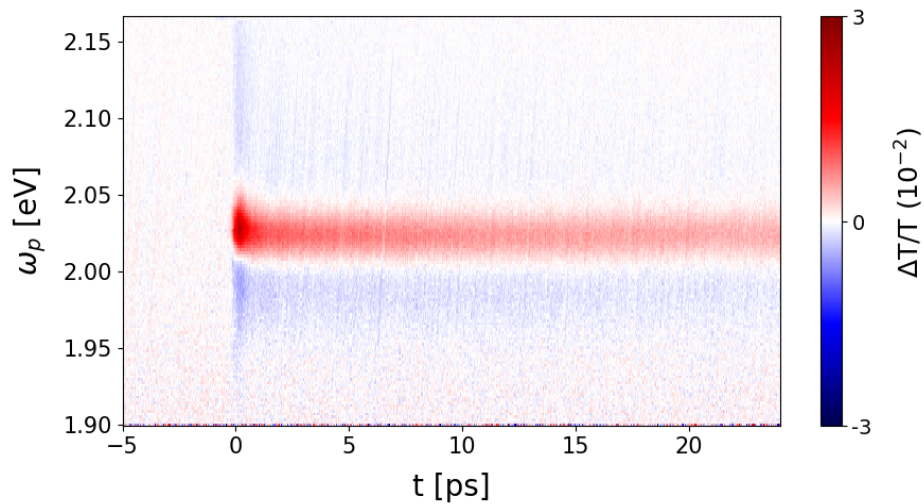


Figure S12: Time- and energy-resolved  $\Delta T/T$  map upon photoexcitation by the visible pump at longer pump-probe delays.



## Supplementary Note 7: Time-resolved Autler-Townes splitting

The measurements of the time-resolved Autler-Townes splitting have been performed according to the conceptual scheme in the rightmost panel of Fig. 1b. In order to simultaneously measure the pump- and the control field-induced changes in the transmittance, we used a differential acquisition based on two synchronized choppers. As detailed in Ref. [36], the visible pump and the mid-IR pulse have been mechanically chopped at frequencies 90 Hz and 45 Hz, respectively. The choppers are seeded by the same wavefunction generator so that their rotations are phase-locked. After the chopper, a small back-reflection of both pulses is routed to a pair of photodetectors to measure the presence/absence of the pump pulse. Since both photodetectors are digitized using the same PCI ADC digitizer (by Spectrum) that acquires pulse-by-pulse the probe and reference spectra, each probe/reference pulse can be assigned with a “label” which indicates the chopper status (ON/OFF). The choppers run one at twice the frequency of the other, so that the probe pulses can fall into four categories according to the status of each chopper: i) both pump pulses are on, ii) only the visible pump excites the sample, iii) only the mid-IR pump excites the sample, iv) no pump interacts with the sample.

To study the pump-induced dynamics, we delayed in time the mid-IR field with respect to the visible pump by the amount  $\Delta t$ . We then scanned the broadband probe in time with respect to the visible pump. For every  $\Delta t$ , the differential acquisition allowed us to compute three types of transient  $\Delta T/T$  maps: one containing the response to both photoexcitations [(i-iv)/iv], one only measuring the changes induced by the visible pump [(ii-iv)/iv] and one measuring the Autler-Townes splitting induced only by the mid-IR field [(iii-iv)/iv].

In Fig. S13a we plot the transient  $\Delta T/T$  maps of the first kind for selected time-delays  $\Delta t$ . For  $\Delta t = -500$  fs (leftmost panel), the mid-IR field impinges on the sample 500 fs before the arrival of the visible pump. At  $t = -500$  fs, the optical signature of the Autler-Townes splitting is clearly visible. From  $t = 0$  fs on, the transmissivity is instead modulated by the interaction with the visible pump, according to

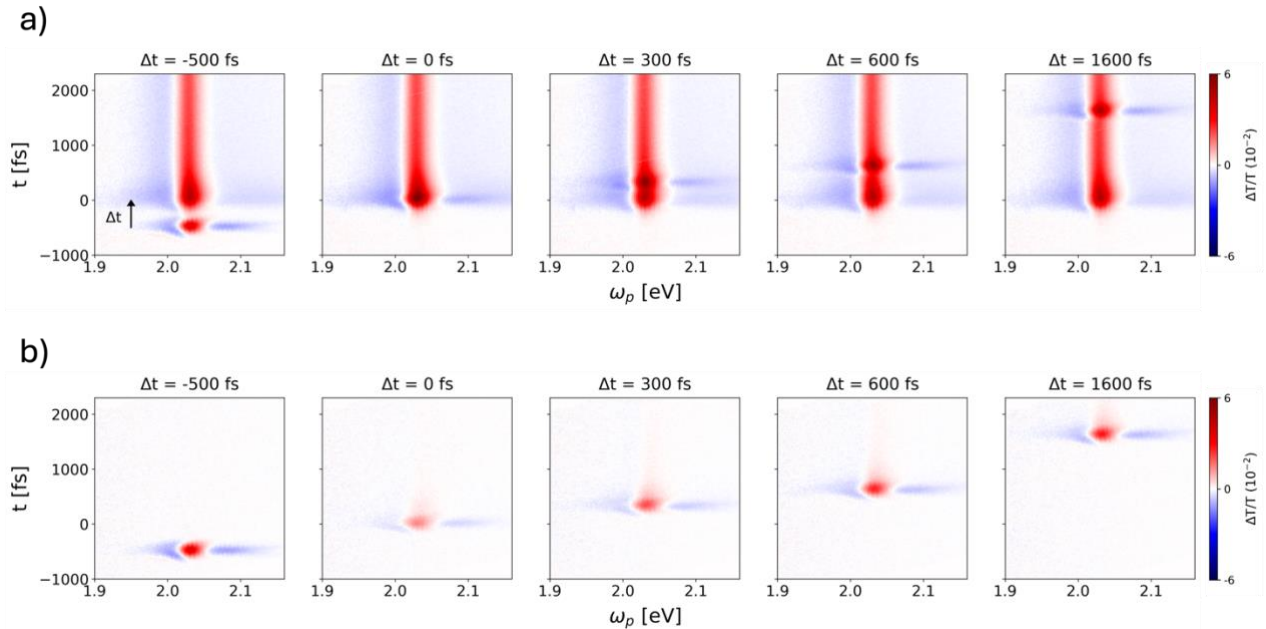


Figure S13: a) Time- and energy-resolved  $\Delta T/T$  maps acquired upon simultaneous excitation by the above-gap pump ( $\omega_{pump} = 3.1$  eV) and the mid-IR control field ( $\omega_c = 155$  meV). The above-gap pump impinges at  $t = 0$ , while the mid-IR field is delayed in time by  $\Delta t$  with respect to it. b) Maps in a) after direct subtraction of the signal associated to the above-gap pump.

the dynamics discussed in the main text (Fig. 4a). At positive  $\Delta t$ , the mid-IR pulse interacts with the sample after the arrival of the above-gap pump.

In order to single out how the Autler-Townes splitting is affected by the excitation by the visible pump, we directly subtract from the maps in Fig. S13a the response associated to the visible pump only [(ii-iv)/iv]. The result of the subtraction is plotted in Fig. S13b. The map at  $\Delta t = -500$  fs is obviously not affected by the subtraction because the mid-IR impinges on the sample before the visible pump. For  $\Delta t \geq 0$ , however, we observe a difference in the Autler-Townes splitting. Notably, we notice a quench of its intensity and a spectral broadening.

These effects are better visualized in the  $\Delta T/T$  spectra plotted in Fig. S14. The colored lines are horizontal cuts of the maps in Fig. S14 at the corresponding time delay between the visible and the mid-IR pumps. To facilitate the comparison, we plot for each curve also the “reference” Autler-Townes spectrum (thin grey line), namely the spectrum acquired in the absence of the above-gap photoexcitation [(ii-iv)/iv]. The transparency window opened by the Autler-Townes effect is quenched by more than 50% at the temporal overlap between the visible pump and the mid-IR field. At larger delays, the intensity is then almost fully recovered.

In order to extract quantitative information on the changes induced by the above-gap pump, we fitted the colored curves (for each time delay) using the complex susceptibility derived in the theoretical model. In particular, we used the following fitting function:

$$\frac{\Delta T}{T}(\Delta t) = \frac{T[\omega_p, \omega_{12}(\Delta t), \gamma_{12}(\Delta t)] - T[\omega_p, \omega_{12}(\Delta t), \gamma_{12}(\Delta t), \Omega_C = 0]}{T[\omega_p, \omega_{12}(\Delta t), \gamma_{12}(\Delta t), \Omega_C = 0]} \quad [\text{Eq. S3}]$$

Which has the same functional form of Eq. S2, but with the important difference that, at each time delay, the central frequency ( $\omega_{12}$ ) and the width ( $\gamma_{12}$ ) of the 1s transition are modified by the above-gap pump. We fed into the fitting function the temporal evolution  $\omega_{12}(\Delta t)$  and  $\gamma_{12}(\Delta t)$  extracted from the fit in Supplementary Note 5, namely the curves plotted in Fig. 4b and 4c. The best fits are plotted as dashed black lines in Fig. S14.

For each time delay, the parameters providing the optimal fit to the data were extracted. The parameter  $\gamma_{13}$ , which was determined to be 65 meV under equilibrium conditions, exhibits only minor modifications under above-gap perturbation, increasing to 75 meV. However, no clear dependence of this parameter on the time delay  $\Delta t$  was observed. In contrast, the parameter most significantly affected by photoexcitation is  $\Delta_C$ , indicating that the energy separation between the 1s and 2p states is dynamically modulated by the interaction with the visible pump. By determining the absolute redshift of the 1s energy level (Fig. 4b), we were able to calculate the corresponding absolute energy shift of the 2p level, as shown in Fig. 5b.

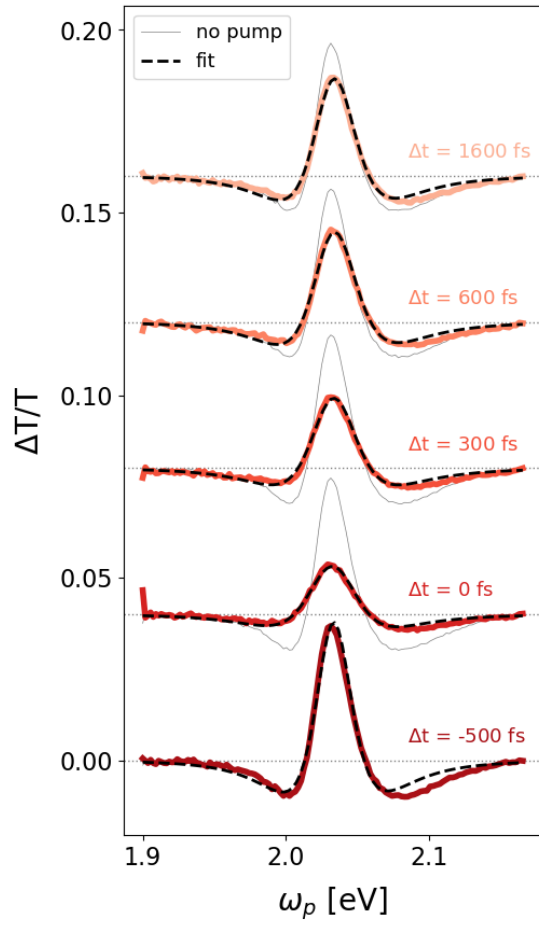


Figure S14: Spectra of the Autler-Townes splitting after the above-gap photoexcitation. Each colored curve corresponds to a different time-delay between the visible pump and the mid-IR control field that measures the splitting. For each delay, the thin grey curve is the splitting measured in the absence of the visible photoexcitation: it is the same for all the  $\Delta t$  and is a reference to enhance the pump-dependent changes. The dashed black line on top of each curve is the fit performed using Eq. S3.